Astronomy & Astrophysics manuscript no. aa
April 25, 2024

Synthetic stellar spectra to study multiple populations in globular clusters:

an extended grid and the effects on the integrated light

Vinicius Branco[1,2], Paula R. T. Coelho[1], Ariane Lançon[2], Lucimara P. Martins[3], and Philippe Prugniel[4]

[1] Universidade de São Paulo, IAG, Rua do Matão, 1226, 05508-090, Sao Paulo, SP, Brazil.
e-mail: vbranco@usp.br
[2] Université de Strasbourg, CNRS, Observatoire astronomique de Strasbourg, UMR 7550, F-67000 Strasbourg, France.
[3] NAT – Universidade Cidade de São Paulo, Rua Galvão Bueno, 868, 01506-000, Sao Paulo, SP, Brazil.
[4] Université de Lyon, LyonI, CRAL-Observatoire de Lyon UMR5574, CNRS, France.

Received Dec. 18, 2023; accepted Apr. 16, 2024.

ABSTRACT

Most Galactic Globular Clusters (GCs) harbour multiple populations of stars (MPs), composed of at least two generations: the first characterized by a "standard" α-enhanced metal mixture, as observed in field halo stars of the Milky Way, and the second displaying anti-correlated CN–ONa chemical abundance pattern in combination with an enhanced helium fraction. Adequate collections of stellar spectra are needed to characterize the effect of such stellar abundance changes on the integrated light of GCs. We present a grid of synthetic stellar spectra covering the atmospheric parameters relevant to old stellar populations at four subsolar metallicities and two abundance patterns, representative of first- and second-generations of stars in GCs. Integrated spectra of populations were computed using our stellar grid and empirical stellar populations, namely, colour-magnitude diagrams from literature for Galactic GCs. The spectra range from 290 to 1000nm, where we measured the effect on several spectrophotometric indices due to the surface abundance variations attributed to MPs. We find non-negligible effects of the MPs on spectroscopic indices sensitive to C, N, Ca, or Na, and on Balmer indices; we also describe how MPs modify specific regions in the near-UV and near-IR that can be measured with narrow or medium photometric passbands. The effects vary with metallicity. A number of these changes remain detectable even when accounting for the stochastic fluctuations due to the finite nature of the stellar population cluster.

Key words. atlases; globular clusters: general; stars: atmospheres; stars: Population II.

1. Introduction

It is currently well-accepted that most Galactic Globular Clusters (GCs) are characterized by multiple populations of stars (MPs). Evidence has been found in color-magnitude diagrams (CMDs) (Piotto et al. 2007; Milone et al. 2013; Milone et al. 2016; Dondoglio et al. 2022; D'Antona et al. 2022), and directly via the spectroscopic determination of star-by-star chemical abundances (Wheeler et al. 1989; Kraft 1994; Kraft et al. 1997; Carretta et al. 2009, 2010). Chemical variations among stars of the same GC are found to be anti-correlated, with one element being depleted while the other is enhanced, such as carbon and nitrogen, oxygen and sodium, and sometimes magnesium and aluminium (Bragaglia et al. 2010; Gratton et al. 2012; VandenBerg et al. 2022). For an extensive study about MPs in GCs and star clusters in general we refer the reader to the reviews by Bastian & Lardo (2018), Gratton et al. (2019) and Krumholz et al. (2019).

If Galactic clusters are local representatives of GCs in general, extragalactic GCs (EGCs) should present the same MP phenomenon. Indeed, GCs outside of the MW have been extensively studied (e.g., Brodie & Strader 2006; Schiavon et al. 2013; Larsen et al. 2014; Nardiello et al. 2018; Salaris et al. 2019; Larsen et al. 2022; D'Abrusco et al. 2022), and the multiple stellar populations have been reported, for example, in the LMC and SMC (e.g., Mucciarelli et al. 2009; Dalessandro et al. 2016; Niederhofer et al. 2017b,a; Hollyhead et al. 2017; Gilligan et al. 2019; Lagioia et al. 2019; Milone et al. 2020; Saracino et al. 2020; Salgado et al. 2022). While the mechanism behind the formation of MPs is still unknown the observed integrated spectra of GCs are frequently used to test simple stellar population (SSP) models (see, Lee & Worthey 2005; Percival et al. 2009; Walcher et al. 2009; Vazdekis et al. 2010; Thomas et al. 2011; Martins et al. 2019). It is not yet clear to what extent using SSP models to represent systems that are not homogeneous in terms of chemical abundances may impact the analysis of extragalactic GCs (e.g. Larsen et al. 2018).

Efforts have also been directed towards searches for signatures of MPs in the integrated light of EGCs. For instance, McWilliam & Bernstein (2008) have determined abundances of several elements for 47 Tuc, finding enhanced Na and Al. Studying 31 GCs from M31, Colucci et al. (2009, 2014, 2017) reported correlations of light element abundance ratios with luminosity and velocity dispersion, evidence of Mg, Na, and Al abundance variations amid GC stars, and that Mg, Al (and likely O, Na) measurements of those EGCs resemble the Galactic GCs. Colucci et al. (2011) reported that old GCs in LMC display higher abundance variations of the light elements Mg, Al, and Na than younger GCs, while Schiavon et al. (2013); Sakari et al. (2016, 2021) report finding that light-element enhancements show positive correlations with EGC mass. Furthermore, studies have measured the chemical abundances (Larsen et al.

2022) and metallicities (Sakari & Wallerstein 2022) of the Local Group and outer halo M31 GCs, respectively.

Regarding the modelling of integrated light, Coelho, Percival, & Salaris (2011, 2012, hereafter "**C11**") were the first to predict how the chemical anticorrelations affect the integrated spectrum of stellar populations. The authors computed integrated stellar populations with both a "standard" α-enhanced metal mixture [α/Fe] $\sim$ 0.4 and with an anticorrelated CN–ONa chemical abundances pattern (with and without He enhancement). They provide a quantitative estimate of the maximum effect that a second population would have on Lick indices, for an iron abundance representative of a typical metal-rich galactic GCs ([Fe/H] = -0.7). Their results indicate that the presence of a 2nd population would increase the equivalent width of some indices (e.g. H_γ, CN_1, CN_2, and NaD) and decrease the equivalent width of others (Ca4226, G4300, and Mg_b). These changes go in the direction needed to explain discrepancies between models and GCs observations when only α-enhancement chemical changes are taken into account in SSP models (Chung et al. 2013). The Balmer lines are affected by the second generation of stars when helium enhancement is considered through the change of the turnoff temperature of the underlying isochrone. This effect would imply that an integrated spectrum could appear up to 2–3 Gyr younger than the true age of the population. Yet, C11 predictions were limited to only one iron abundance and the wavelength range 3500 to 6000 Å. The effects on a wider range of metallicities and observables remain to be explored.

In the present work, we aim to expand the study performed by C11, by making a grid of synthetic stellar spectra available for a wider range of metallicities and wavelengths, both for a standard α-enhanced metal mixture and for a composition characteristic of second populations of globular clusters. The spectra are computed with an optimized combination of existing line lists. They are used to predict the effects of MPs on the integrated spectra of old clusters and spectrophotometric indices, as a function of metallicity. Because globular clusters contain only a finite number of stars, clusters of a given age, composition, and mass can randomly display a range of integrated properties (e.g. Barbaro & Bertelli 1977; Bruzual A. 2002; Fouesneau & Lançon 2010; Popescu & Hanson 2010; da Silva et al. 2012). We examine to what extent the effects of MPs remain detectable in that stochastic context.

This paper is organized as follows: in Section 2 we present the synthetic stellar grid, and in Section 3 we describe how the integrated stellar population models were built. We simulate the stochastic populations in Section 4, and discuss the results of measured properties in Section 5. Our concluding remarks are given in Section 6.

2. Synthetic stellar spectra with abundances representative of globular cluster stars

We computed a grid of synthetic stellar spectra suitable for modelling integrated SSPs with old ages, subsolar metallicities, and chemical abundance patterns relevant to globular clusters. Here, we describe the codes and ingredients used and the properties of the final grid.

2.1. Ingredients and codes

The model atmospheres and the synthetic spectra were computed with the Linux ports of `ATLAS12` and `SYNTHE` codes, respectively (Kurucz 1970, 2005; Kurucz & Avrett 1981; Kurucz & Furenlid 1979; Sbordone et al. 2004; Sbordone 2005). These are the same codes adopted in C11 and have been used recently in the study of the integrated data of GCs (Jang et al. 2021; Larsen et al. 2022). For each chemical mixture pattern adopted in this project, we computed both the model atmosphere and the synthetic spectrum.

Our atmosphere models were computed using the Opacity Sample method under LTE conditions and 1-D plane-parallel geometry. The models were calculated assuming the microturbulence of 1 km/s, 60 iterations, 72 layers, mixing length parameter of 1.25, and no overshooting. We adopted the same convergence criteria as Mészáros et al. (2012) for the model atmospheres: the layers are tested to have the difference in flux and the flux derivative errors to be less than 1% and 10%, respectively; no more than one non-converged layer was accepted between $\log \tau_{\rm Ross} = -5$ and $\log \tau_{\rm Ross} = 1$, where $\tau_{\rm Ross}$ is the Rosseland optical depth.

The synthetic spectra were computed with a sampling resolution of 1 700 000, convolved with a Gaussian filter to a spectral resolution of R = 850 000, from 290 nm to 950 nm in the air wavelength. Molecular opacities were obtained from R. Kurucz, covering the following molecules: AlH [A-X], AlH [B-X], AlO, C_2 [A-X], C_2 [B-A], C_2 [D-A], C_2 [E-A], CaH, CaO, CH, CN [A-X], CN [B-X], CN [X-X], CO [A-X], CO [X-X], CrH [A-X], FeH [F-X], H_2, MgH, MgO, NaH, NH, OH, SiH, SiO [A-X], SiO [E-X], SiO [X-X], TiH, TiO, and VO [1]. We compiled a new atomic opacity list based on three lists available in the literature, described in section 2.2. The chemical patterns of the grid are discussed in section 2.3.

To automatise the process of computing the grid, we developed a `Python` wrapper called "Python Globular Cluster Synthesizer" (hereafter, `PyGlobsterS`), which combines the `ATLAS12` and `SYNTHE` executions and the integration of the SSP spectra (described later in Section 3). `PyGlobsterS` decreases the time consumed to compute a large sample of models by allowing it to run in parallel jobs.

2.2. Optimisation of the atomic line list

Different opacities can significantly impact the quality of the synthetic spectrum. Martins & Coelho (2007), for example, tested the accuracy of stellar libraries that assume different opacities and codes, observing that the library with the best average performance employed an atomic line list calibrated against the spectra of the Sun and Arcturus. Recent studies have pointed out the need for accurate opacity lists, not only to describe stars on different evolutionary stages but also different regions of the wavelength range (e.g., Martins et al. 2014; Franchini et al. 2018; Lançon et al. 2021).

Based on the purpose of this work, we focused on compiling a list based on literature sources that were available in the format required by `SYNTHE`: Coelho (2014) (hereafter, "**Coelho14**"), Kurucz (2018)[2] (hereafter, "**Kurucz18**"), and an updated version of the list by Castelli & Hubrig (2004)[3] (hereafter, "**Castelli16**", corresponding to the version of Feb 18th, 2016).

We computed one synthetic solar spectrum for the three atomic lists, keeping the same molecular opacities unchanged.

[1] `http://kurucz.harvard.edu/linelists/linesmol/` (see Table A.1 in the Appendix A and Branco (2020) for details.)
[2] Downloaded from `http://kurucz.harvard.edu/linelists/gfnew/gfall08oct17.dat` on Aug 8th, 2018.
[3] Downloaded from `http://wwwuser.oats.inaf.it/castelli/linelists.html` on Aug 8th, 2018.

In future work, we plan on expanding this study to newer literature on atomic opacities, which were yet to be available when this project started (Larsen et al. 2022; Peterson & Kurucz 2022).

The Sun was chosen as the reference star given its well-defined stellar parameters and high spectral resolution data available in the literature. We considered three determinations for the solar abundances: Grevesse & Sauval (1998), Asplund et al. (2005), and Asplund et al. (2009). All solar models adopt $T_{\rm eff}$ = 5777 K, log g= 4.4377 (Cox 2000, 4th. Ed.) and $V_{\rm turb}$ = 1.0 km/s (Castelli & Kurucz 2003).

The synthetic solar spectra were compared against the solar spectrum obtained from Wallace et al. (2011). This is a high-quality solar spectrum obtained with the Fourier transform spectrometer (FTS) at the McMath-Pierce telescope (as described in Brault 1985) which covers the wavelength region from ~2958–9250 Å with resolution varying from $R = \lambda / \Delta\lambda$ ~350,000–700,000, distributed in six regions (see Table 1 in Wallace et al. 2011). It is a ground-based spectrum corrected for the effect of telluric lines.

We convolved the synthetic spectra to the relevant spectral resolution and used the following metric to quantify the differences between the models and the solar spectrum:

$$\widetilde{\Delta}(\lambda) = \frac{1}{N}\sum_{\lambda_1}^{\lambda_2}\left|\frac{f_{\rm synt}(\lambda_i) - f_{\rm obs}(\lambda_i)}{f_{\rm obs}(\lambda_i)}\right| \quad (1)$$

where N is the number of pixels in wavelength interval $\Delta\lambda = \lambda_2 - \lambda_1$ centred at λ, and $f_{\rm synt}(\lambda_i)$ and $f_{\rm obs}(\lambda_i)$ are the synthetic and observed flux, respectively, at the i-th element of wavelength.

In Figure 1 we show the solar spectra computed with the different line lists and $\widetilde{\Delta}$ as a function of wavelength, to illustrate the behaviour around CaII H&K (top), Mg T (middle), and Na D (bottom). In general, as the wavelength increases, $\widetilde{\Delta}$ decreases.

To choose between line lists we compared the synthetic spectra with the observed solar spectrum over small wavelength intervals of $\Delta\lambda$ = 0.2 Å. For each spectral segment we used equation (1) to select the list which best reproduced the solar spectrum (i.e. lowest $\widetilde{\Delta}$). The best lists of each segment were combined into a new list covering the whole wavelength interval of the observed spectrum. Table 1 summarises the global performance of each line list (i.e. the $\widetilde{\Delta}$ computed over the wavelength range 2958–9250 Å), for three solar abundance patterns. Because the variation among the solar patterns is comparable, we decide to use the most recent reference in the remainder of this article, i.e. Asplund et al. (2009).

2.3. Parameter coverage in the Kiel plane

We aim at a grid of synthetic spectra suitable to represent GCs of different subsolar metallicities. The grid's coverage of the Kiel plane ($T_{\rm eff}$ vs. log g) is based on Milky Way GCs selected from Martins et al. (2019, hereafter "**M19**"), who have translated empirical CMDs from Piotto et al. (2002) into the $T_{\rm eff}$ vs. log g plane using the colour transformations from Worthey & Lee (2011). The CMDs were observed with the WFPC2 camera of the Hubble Space Telescope. The PC was centred in the centre of the clusters and covered a field-of-view of about 2.5' x 2.5'.

Based on the CMDs of NGC 1904, NGC 5904, NGC 0104, and NGC 5927, respectively, we computed synthetic spectra for the metallicities [Fe/H] = –1.60, –1.29, –0.77, and –0.47 (see Table 2 for metallicity references). The coverage in $T_{\rm eff}$ and log g are shown in Figure 2. We consider this coverage appropriate

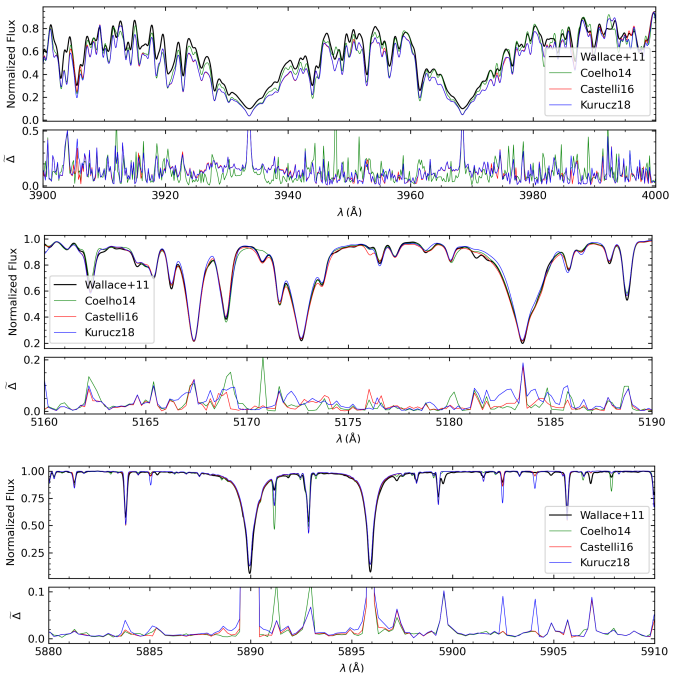

Fig. 1. Comparison between modelled and observed spectra (top panels) and their $\widetilde{\Delta}$ (bottom panels) in three regions: CaII H&K (top), Mg T (middle), and Na D (bottom). Each panel shows synthetic spectra computed with Coelho14 (green), Castelli16 (red), and Kurucz18 (blue) atomic line lists compared to the observed solar spectrum. $\widetilde{\Delta}$ is computed according to Eq. 1 with $\lambda_2 - \lambda_1$ = 0.2 Å.

as Sakari et al. (2014) has shown that the integrated properties are not strongly sensitive to the parameter binning in the HR coverage unless the binning is very coarse. Basic data of the selected clusters are shown in Table 2.

For each [Fe/H], we considered two chemical abundance patterns:

- a standard metal mixture with [α/Fe] ~ 0.4 and initial He mass fraction Y = 0.256, as representative of the first generation (hereafter "**1P**"), and;
- a second generation whose metal composition has C decreased by 0.30 dex, N increased by 1.20 dex, O decreased by 0.45 dex, and Na increased by 0.60 dex with respect to the first generation α-enhanced mixture, with Y = 0.300 (hereafter "**2P**"). The chemical abundances of the grids are summarised in Table 3.

These choices follow the chemical patterns adopted in C11 on the modelling of a typical metal-rich Galactic GC. They were chosen by those authors based on Carretta et al. (2005) to represent values close to the upper end of the observed anticorrelation in Galactic GCs and ensure that both populations have the same C+N+O sum to match the assumption of their adopted isochrones.

To keep the assumptions of the grid homogeneous, we adopted the same abundances of CNONa and He in 2P for all the GCs in Table 2. The chosen upper values of CNONa abundances are appropriate for a range in [Fe/H] from -2.0 to -0.7 dex (as of Carretta et al. 2005) but may be an extrapolation for our most metal-rich GC.

The synthetic stellar spectra are available in the POLLUX database[4] and `http://specmodels.iag.usp.br`.

[4] `https://pollux.oreme.org/`

Table 1. Global performance of each synthetic spectrum computed with different atomic line lists and different solar abundance patterns, according to the metric in Equation 1. $\Delta\lambda$ corresponds to 2958–9250 Å, the wavelength range of the observed solar spectrum.

Solar Pattern	$\widetilde{\Delta}$ Castelli16	$\widetilde{\Delta}$ Coelho14	$\widetilde{\Delta}$ Kurucz18	$\widetilde{\Delta}$ This Work
Grevesse & Sauval (1998)	0.9861	0.9894	0.9895	0.9777
Asplund et al. (2005)	0.9842	0.9884	0.9876	0.9763
Asplund et al. (2009)	0.9856	0.9891	0.9891	0.9771

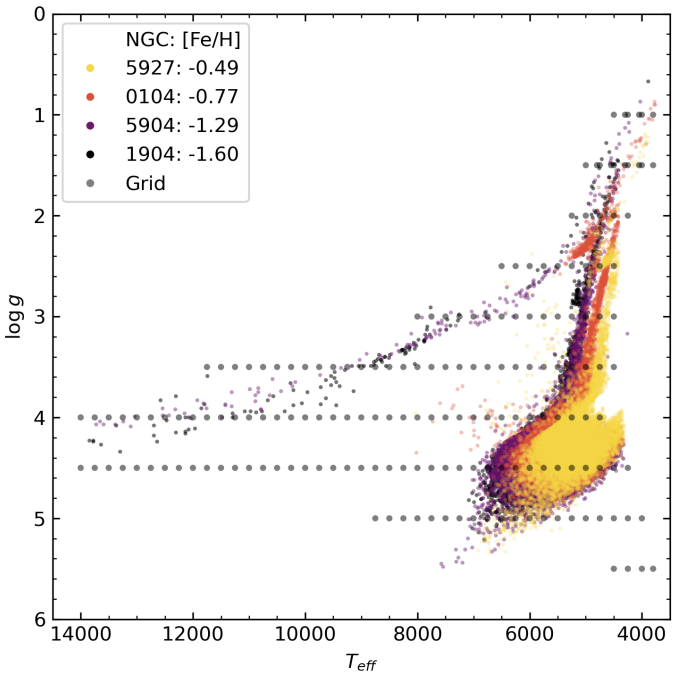

Fig. 2. HRD estimated by Martins et al. (2019) based on observations from Piotto et al. (2002) for NGC5927, NGC0104, NGC5904, and NGC1904, represented by the colored dots. Grey dots indicate the computed spectral models.

Table 2. Globular clusters selected to guide the atmospheric parameter coverage. References: (a) Harris (1996, 2010); (b): Dotter et al. (2010); (c): De Angeli et al. (2005); (d) Carretta et al. (2009); (e) Usher et al. (2017); (f) Projected core radius in arcmin (Harris 1996, 2010).

GC	[Fe/H]	Age	$\log M/M_{\odot}$ [(e)]	R_c
NGC 5927	$-0.49^{(a)}$	$12.2^{(b)}$	5.4	22
NGC 0104	$-0.77^{(d)}$	$12.8^{(b)}$	6.0	10
NGC 5904	$-1.29^{(a)}$	$12.2^{(b)}$	5.8	26
NGC 1904	$-1.60^{(a)}$	$13.0^{(c)}$	5.4	25

3. Application to integrated spectra

We computed integrated spectra of stellar populations following the method proposed by M19 (see as well Schiavon et al. 2004; Colucci et al. 2011; Sakari et al. 2014). In short, data from a CMD is converted to the Kiel plane ($T_{\rm eff}$ vs $\log g$) via a color-$T_{\rm eff}$ transformation. Each star in the Kiel plane is associated with a model in the stellar synthetic grid (the model that is closest to the observed star in atmospheric parameters, see equation 3 in M19). The integrated spectrum is obtained by summing up the individual model spectra, weighted by the magnitude M_V of the corresponding observed stars.

This approach has the advantage of avoiding uncertainties related to the IMF and isochrones modelling. On the other hand, it has the disadvantage of being sensitive to the sampling of luminous stars and rapid phases, incompleteness of low-mass stars, and mass segregation if present (see e.g. McWilliam & Bernstein 2008), as the CMD will rarely (if ever) cover the entirety of the GC stars. The CMDs we use in this work were observed with the WFPC2 camera with the PC centred on the cluster centre (Piotto et al. 2002). Considering the core radius of the GCs in Table 2, our models are representative of the central parts of the GCs populations.

The integrated flux F_λ of N stars is given by:

$$F_\lambda = \sum_{i=1}^{N} f_{\lambda,i} C_i \tag{2}$$

where f_λ is the spectrum of i-th star, and C_i is the weight of the i-th star, defined as:

$$C_i = \frac{10^{\frac{-M_{V,i}}{2.5}}}{\int T^V_\lambda f_{\lambda,i} d\lambda}. \tag{3}$$

where $M_{V,i}$ is the absolute magnitude of the i-th star, and T^V_λ is the response function of the V-band filter.

For each metallicity and chemical pattern we computed an integrated spectrum, resulting in eight synthetic SSPs. By modelling two simple populations for each iron abundance with extreme chemical pattern values (pure 1P and pure 2P), we aim to estimate an approximate upper level of changes in spectrophotometric features due to CNONa and He variations, rather than to model real GCs. Future work will relax these assumptions to consider varying degrees of chemical changes and 1P/2P proportions (or intermediate subpopulations) as a function of metallicity (Carretta et al. 2009), mass (Schiavon et al. 2013), and radius (Sakari et al. 2014).

The resulting integrated spectra are shown in the left-side panel in Figure 3. As expected from the CMDs, the spectral energy distribution of the two most metal-poor cases shows the Balmer features caused by the strong contribution of relatively hot horizontal branch stars. The right-side panel of the figure shows the ratio between the 2P and 1P reference spectrum for each iron abundance. As can be seen from this panel, the effect of the chemical variations is stronger in the blue region, corresponding to molecules CH, OH, and NH. A feature corresponding to the Na D line is in 5800 Å. Redder than 7000 Å, the signal corresponds to CN molecular band.

The highlighted regions in the right-side panel in Figure 3 correspond to wavelength windows with a strong sensitivity to the presence of 2P and are discussed later in Section 5.

4. Simulating stochastic populations

Globular clusters may differ by their global physical parameters such as age, metallicity, stellar mass, detailed star formation history, and relative fraction of 1P and 2P stars. But even

Table 3. Chemical abundance patterns for each SSP. **Y** is the normalized mass fractions of He; **H** to **Na** are abundances as used in `ATLAS12` (H and He are linear number fractions, and C, N, O, and Na are number fractions in logarithmic scale).

Grid	[Fe/H]	[α/Fe]	Mixture	Y	H	He	C	N	O	Na
I	-1.58	0.4	1P	0.256	0.92015	0.07980	-3.61	-4.21	-2.95	-5.80
II	-1.58	0.4	2P	0.300	0.90246	0.09749	-3.91	-3.01	-3.40	-5.20
III	-1.29	0.4	1P	0.256	0.92003	0.07987	-3.61	-4.21	-2.95	-5.80
IV	-1.29	0.4	2P	0.300	0.90233	0.09757	-3.91	-3.01	-3.40	-5.20
V	-0.77	0.4	1P	0.256	0.91951	0.08017	-3.61	-4.21	-2.95	-5.80
VI	-0.77	0.4	2P	0.300	0.90174	0.09793	-3.91	-3.01	-3.40	-5.20
VII	-0.47	0.4	1P	0.256	0.91877	0.08059	-3.61	-4.21	-2.95	-5.80
VIII	-0.47	0.4	2P	0.300	0.90090	0.09844	-3.91	-3.01	-3.40	-5.20

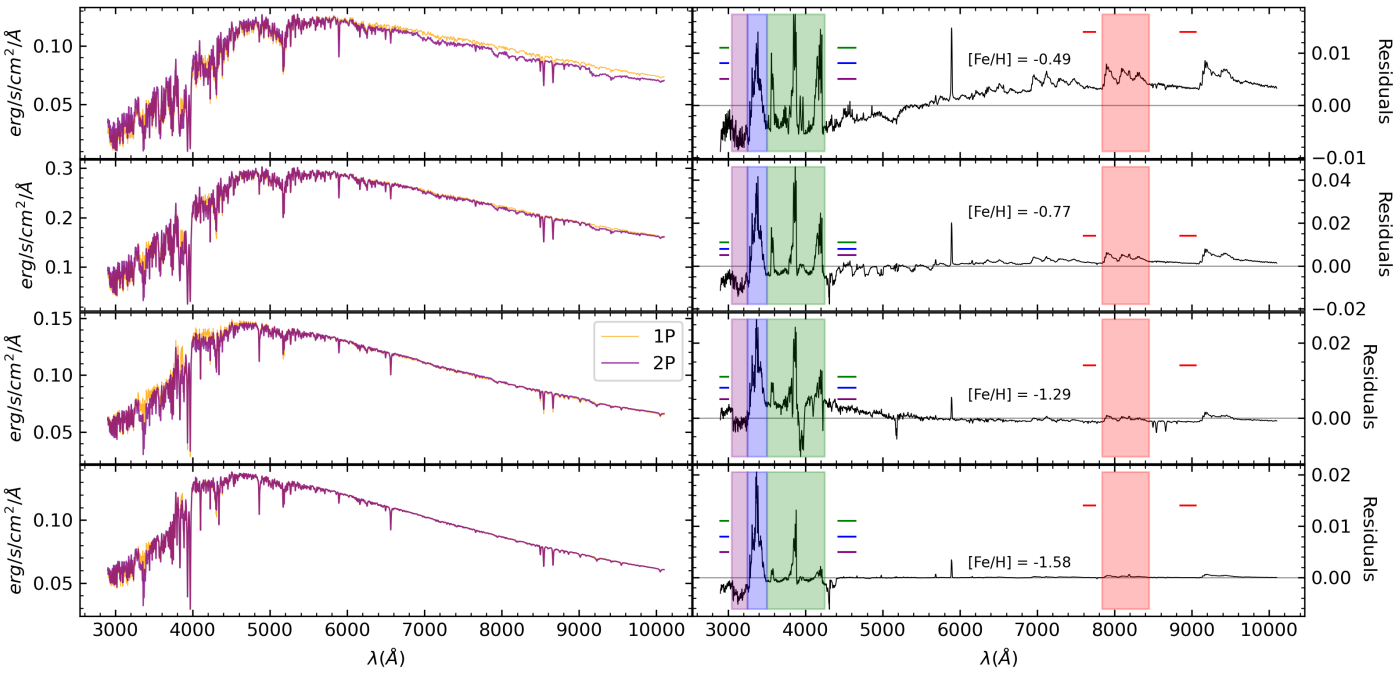

Fig. 3. Left-side panel: The model SSPs are shown. "Gen.1" indicates models with the standard mixture of the "first generation", i.e., "α-enh". "Gen.2" represents the modified mixture of a "second generation", i.e. "α– and Y–enhancements and ΔCNONa" (it also considers the CN–ONa abundance variations). The iron abundances are indicated in the texts on the right panels. Right-side panel: The residual flux between 1st and 2nd generation spectra, for each iron abundance. The wavelength regions affected by the chemical variations typical of the 2nd generation are seen, corresponding to changes in the CH/OH/NH and CN bands and Na D line strength. Coloured lines indicate the blue and red continua bandpass intervals that correspond to the central bandpass areas of the same colour.

clusters with the same physical parameters might have different integrated emission spectra due to the stochastic nature of the actual distribution of their finite number of stars. The smaller the total mass of the cluster, the larger the relative fluctuations in observational properties, such as colours and spectroscopic indices (e.g. Fouesneau & Lançon 2010; Cerviño 2013). Here, we aim to examine to what extent the effects of MPs on the integrated light remain detectable in this stochastic context. To that end, we simulate stochastic populations in each of the synthetic SSPs and repeat the comparison between 1P and 2P.

The relative amplitude of stochastic fluctuations depends on the size (total stellar mass) of the stellar population considered, and that size varies among our four Milky Way GC datasets. Most of the variance comes from bright and short-lived phases, such as the AGB at red or near-infrared wavelengths, or the HB at blue wavelengths, when the HB is extended. In order to bring the four GCs to a common scale, we need to normalize the CMDs to have the same number of stars in a chosen magnitude range. We choose the upper limit of the luminosity range to be the Turn-Off point (TO) because the sampling of MS stars is stable against stochastic fluctuations. Regarding the lower luminosity limit, we should consider that Piotto et al. (2002) observations are magnitude-limited and therefore each CMD reaches different depths in the faint MS (closer GCs reach lower masses in the MS). We chose to limit the faintest star to be considered for normalization to the star closest to V(TO) + 1. Therefore we split each CMD into two sub-samples:

- "subsample A" includes the stars from the TO down to 1 magnitude fainter, i.e. $V(\mathrm{TO}) \leq V_{star} \leq V(\mathrm{TO})+1$: this range is stable against stochastic fluctuations and is used to normalize the number of stars across the four CMDs;
- "subsample B" span all stars brighter than the TO ($V_{star} < V(\mathrm{TO})$): this is the range which causes the stochastic fluctuations in the observables (colours and/or indices).

We obtain the position of the TO (that splits subsample A and B) from the V-magnitude predicted from isochrones taken

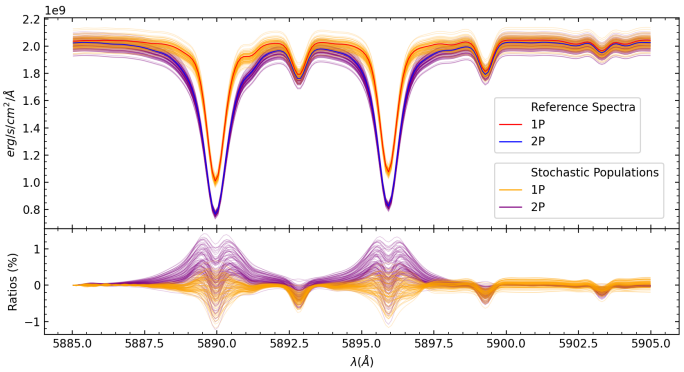

Fig. 4. Top: Stochastic effect in the Na D spectral line of the reference integrated spectra for 1P (blue) and 2P (red) and [Fe/H] = −0.77. The bootstrapped populations of each mixture are shown, respectively, in orange and purple. Bottom: ratios and residuals between bootstrapped and reference integrated spectra.

from "a Bag of Stellar Tracks and Isochrones" (BaSTI; Hidalgo et al. 2018; Pietrinferni et al. 2021)[5]. For each GC, we requested an isochrone with the appropriate cluster age, iron abundance interpolated to that of the target cluster, α-enhancement ([α/Fe] = 0.4), and photometry in the Johnson-Cousins photometric system. Ages and iron abundances adopted are those in Table 2. For the helium mass fraction (Y), we adopted 0.247 and 0.300 for 1P and 2P, respectively.

To relate the number of stars in subsample A to the total number of stars in the cluster, we assumed that the initial stellar mass function (IMF) can be approximated with the universal function of Kroupa (2001). That assumption also allows us to compute an expected number of stars in the initial mass interval associated with subsample B. The latter is (not surprisingly) not precisely equal to the actual number of stars observed in subsample B. We run simulations of SSPs drawing stars from the CMDs, with the constraint that every population has the same total number of stars to be integrated. We also set that the proportion of stars between subsamples A and B is obtained from the IMF.

Table 4 presents the quantities used to compute the number of stars. In subsample A, we use the stellar mass of the Turn-Off M_{ini}(TO) and the stellar mass of a star which is 1 magnitude fainter $M_{ini}(V(\mathrm{TO})+1)$. In subsample B, we use the stellar mass in the Turn-Off M_{ini}(TO) and the initial mass at the beginning of the TP-AGB phase M_{ini}(TP-AGB).

For each SSP in Table 4 we built 100 simulated populations, each with 20 000 stars in the mass range between $M_{ini}(V(\mathrm{TO})+1)$ and M_{ini}(TPAGB), to be representative of GCs with total masses $M \approx 10^5 M_\odot$ For subsample A, we bootstrapped the stars only once given that the contribution of these stars is very stable. For subsample B, we bootstrapped the stars 100 times, one for each simulated population. The ratio between the two subsamples is fixed, based on the IMF.

Therefore, each mixture and metallicity has one hundred bootstrapped populations, normalized to the same total number of stars. Figure 4 illustrates the effect of the stochasticity on the Na D spectral line for the two chemical mixtures of the metallicity regime relative to NGC 0104, 47Tuc, [Fe/H] = −0.77. Both the strength and the profile of these strong lines are sensitive to the exact sampling of the stellar mass function. The stochastic effects on the spectrophotometric indices sensitive to the MP are discussed in the next section.

[5] `http://basti-iac.oa-abruzzo.inaf.it/isocs.html`

5. Results and discussion

We evaluate the effect of abundance variations between 1P and 2P and related stochastic effects via spectroscopic (Trager et al. 1998) and photometric indices (Milone et al. 2016). All measurements were made with the Python package `PYPHOT` [6] (Fouesneau 2022).

5.1. Indices sensitive to multiple populations

The work of C11 identifies the Lick indices that are most sensitive to the presence of a 2P, namely CN_1, CN_2, Ca4227, G4300, and Na D. We computed these indices in our models for [Fe/H] = −0.77 (the only metallicity explored in C11) and compare the results in Table 5.

The differences between 1P and 2P from C11 and this work differ in absolute values but show the same trend. Since the codes are the same between the two works, we attribute the difference to the opacities. Regarding the molecular opacities, we used Masseron et al. (2014) opacity table for the CH molecule, which is more up-to-date than the one used in C11. Our atomic line list has been refined from literature, as explained in section 2.2.

Inspired by C11 and based on Figure 3, we proposed four new spectral regions predicted to be sensitive to the CH, CN, OH, and NH molecular features in the integrated light. The regions were selected by visually inspecting the ratio between 1P and 2P integrated spectra, shown in the right-side panel of Figure 3. The features are listed in Table 6, in terms of the usual blue, central, and red bandpasses used in Lick/IDS indices (e.g. Worthey et al. 1994). The index names OH_{blue}, NH_{blue}, CN_{blue}, and CN_{red} refer only to the dominant species in the central passband (see Fig. 15 in Coelho et al. 2005), and they are represented in Figure 3 by the pink, purple, green and red colours, respectively. The NH index is a narrow-band measurement of the spectral feature also measurable with Hubble Space Telescope filters, for instance with the 3-filter index of Milone et al. (2013) now used commonly to produce so-called "chromosome maps". All measured standard Lick indices, as well as other relevant indices from the literature, can be found in Table B.1, and we further discuss their behaviour in the next section.

5.2. The effects across different metallicities

Figure 5 shows index-index diagrams with the populations computed in this work. Each panel shows a spectral index from those identified by C11 to be strongly sensitive to MPs *versus* the metallicity-sensitive index Fe5270. Each dot in the diagrams is a bootstrapped population (section 4).

We confirm the results by C11 that the indices CN_1, CN_2, Ca4227, G4300, and Na D are sensitive to the presence of MPs[7]. We also identify that the difference between the 1P and 2P models, represented by the line strengths in the index-index diagrams, generally increases with metallicity. This result is supported by Sakari et al. (2016, 2021) where the increasing Na D line strength indicates an increasing Na-enhanced stellar abundance. The stochastic effect together with typical measurement errors at the two lowest metallicities prevents the separation between 1P and 2P for the indices CN_1, and G4300. At higher metallicities and in the case of Na D, and Ca4227, the separation between 1P and 2P seems to be robust against stochasticity.

[6] `https://mfouesneau.github.io/pyphot/index.html`

[7] For conciseness we show CN_1 but not CN_2, which behaves very similarly.

Table 4. Data obtained from the isochrones to compute the ratio between subsamples A and B. Reference metallicity and chemical mixtures are presented in the first two columns. From the third column on, we show the data obtained from the isochrones: absolute V magnitude in the Turn-Off [V(TO)] and its stellar mass [M_{ini}(TO)]; absolute V magnitude of the nearest neighbor star 1 magnitude fainter than the Turn-Off [V(TO) + 1] and its initial mass [$M_{ini}(V(\mathrm{TO})+1)$]; absolute V magnitude of a star at the beginning of the TP-AGB phase [V(TP-AGB)] and its initial mass [M_{ini}(TP-AGB)].

Metallicity	Mixture	V(TO)	M_{ini}(TO)	V(TO) + 1	$M_{ini}(V(\mathrm{TO})+1)$	V(TP-AGB)	M_{ini}(TP-AGB)
-0.49	1P	4.75	0.879	5.75	0.796	-1.08	0.965
-0.77		4.74	0.819	5.73	0.742	-1.43	0.891
-1.29		4.51	0.773	5.51	0.704	-1.86	0.830
-1.60		4.42	0.756	5.41	0.694	-1.93	0.800
-0.49	2P	4.83	0.822	5.82	0.744	-1.13	0.899
-0.77		4.86	0.753	5.85	0.683	-1.47	0.819
-1.29		4.59	0.708	5.59	0.646	-1.86	0.756
-1.60		4.51	0.692	5.49	0.638	-1.88	0.730

Table 5. Variations of Lick indices for [Fe/H] = −0.7 as in C11 ($\Delta I_{\mathrm{Coelho}}$) and those calculated in this work ($\Delta I_{\mathrm{ThisWork}}$), between 1P and 2P.

Index	$\Delta I_{\mathrm{Coelho}}$	$\Delta I_{\mathrm{ThisWork}}$
CN_1	0.084	0.050
CN_2	0.087	0.052
Ca4227	-0.651	-0.227
G4300	-0.572	-0.813
Na D	1.346	0.785

Table 6. New indices proposed to be sensitive to the MP effects in GCs. The bandpasses are defined in angstroms (Å) and indices are measured in magnitudes.

	Bandpasses		
	Blue	Central	Red
OH_{blue}	2900 – 3000	3050 – 3250	4430 – 4650
NH_{blue}	2900 – 3000	3250 – 3500	4430 – 4650
CN_{blue}	2900 – 3000	3510 – 4250	4430 – 4650
CN_{red}	7600 – 7750	7840 – 8450	8850 – 9050

In any case, one should be aware that our simulated 1P and 2P are ideal cases illustrating the maximum separations, while in integrated extragalactic GCs we will observe a mixture of populations.

Regarding our proposed indices, we show in Figure 6 that some combinations of indices are robust against the stochastic effects. OH– and NH–Fe5270 diagrams do distinguish them well. CN_{red} effectively split the two mixtures at high metallicity regimes, despite the high dispersion due to stochasticity in low metallicities. CN_{blue} has tighter splits in the high metallicities compared to its red counterpart, being not as effective as the other indices.

In Figure 7, we draw attention to the OH–NH diagram (top-left panel), where the groups are well separated. Something similar happens when comparing OH or NH with CN_{red} or CN_{blue}, as in the diagrams of the second row.

We point out the work by Bertone et al. (2020) where a set of new spectral indices was also proposed to identify the MP effects. These authors performed a star-to-star comparison at different evolutionary stages, with four chemical mixture assumptions for a metallicity [Fe/H] = −1.62; they did not directly examine the indices expected for the integrated light of a cluster. Our methods for producing spectra are slightly different regarding the opacity tables and `ATLAS` version (`ATLAS9` there vs. `ATLAS12` here). Their synthetic spectra, also computed with `SYNTHE`, cover a smaller wavelength interval at lower spectral resolutions; our OH_{blue} index (Table 6) lies outside that interval. In Appendix C we present a set of plots with Bertone et al. (2020) spectral indices computed with the integrated spectra of our bootstrapped populations in Figure C.1, as well as the measurements in Table C.1. We show that their spectral indices, designed to split individual stars of sub-populations, also split 1P and 2P of integrated populations of stars in almost every case.

In Figure 8, we show a set of diagrams with the bootstrapped populations for each metallicity and chemical mixture that splits 1P and 2P mixtures using HST filters as suggested in Milone et al. (2013). In the left panel, the color-color diagram uses filters that enhance the separations between populations, in the MS and RGB. The middle panel is a chromosome map based on the pseudo-color index c(F275W,F336W,F410M)[8] that intends to maximize the separations. In this panel, instead of filter F410M, we used F438W in the combination, along with the (mF275W − mF438W) colour, and this change augmented the separations. After exploring more combinations with the HST filters, we suggest a pseudo-colour diagram with two three-filter indices, c(F275W,F336W,438W) vs c(F275W,F438W,F814W) , in the right panel. This diagram splits 1P and 2P with less superposition of the bootstrapped populations thus providing a significant opportunity for measurements of these colours for characterizing the MPs using the integrated light of GCs. Such photometric indices, among others, are commonly used to identify the presence of MPs in colour-magnitude diagrams of galactic GCs (Gontcharov et al. 2023; Milone et al. 2023a), and have been recently applied to the infrared region with the JWST (Milone et al. 2023b; Ziliotto et al. 2023).

6. Conclusions

The multiple population phenomenon in GCs is an exciting entry point for studying these astrophysical objects. To support such studies, we publish a grid of synthetic stellar spectra at four iron abundances and two chemical abundance patterns that characterize GC stars: a standard alpha-enhanced mixture and a mixture with anticorrelated CNONa abundances and He enhancement.

Using these spectra, we have modelled a total of eight integrated spectra of old stellar populations, a pure 1P and a pure 2P

[8] Defined as (mF275W − mF336W) − (mF336W − mF410M).

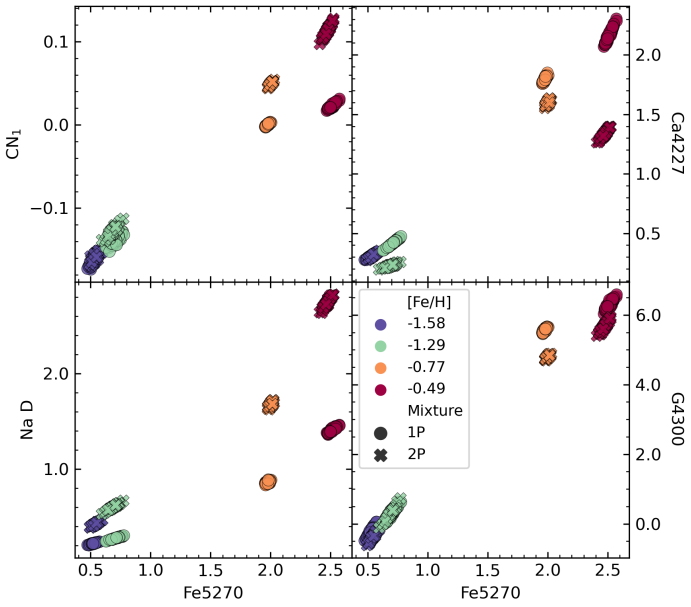

Fig. 5. The stochastic effects in the spectral indices CN_1, Ca4227, G4300, and Na D. Each point in the index-index diagrams corresponds to a population composed of 20,000 stellar models. Each diagram shows 100 populations computed in four metallicity regimes (coloured symbols) and two chemical mixtures (1P and 2P, rounded and x symbols, respectively).

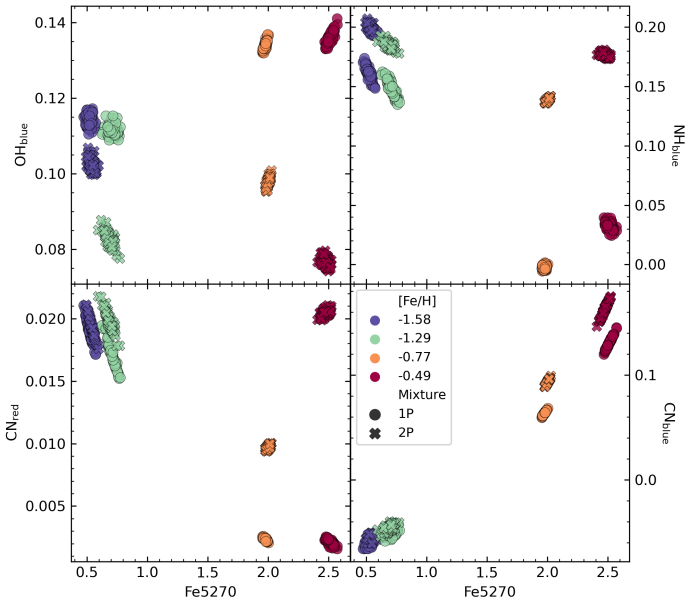

Fig. 6. Same as in Figure 5; this figure presents the stochastic effects in the new indices proposed to be sensitive to the MP effects in GCs as a function of the metallicity: OH_{blue}, NH_{blue}, CN_{blue}, CN_{red}.

per iron abundance. The synthesis of the integrated light is based on colour-magnitude diagrams of Milky Way globular clusters and, therefore, quantifies the effect of GC-specific abundance changes on spectra without accounting for changes in stellar evolution that accompany big changes in the He abundance. We will address the effects of changes in isochrones in a forthcoming work.

We quantified the effect of different chemical mixtures on spectroscopic indices and narrow/medium photometric passbands, accounting for the stochastic nature of real stellar populations. The effect due to the presence of 2P is detectable in many spectrophotometric indices, and the effect is stronger with increasing iron abundance. In low-metallicities, the stochastic nature of the integrated light of GCs will hamper the detection of the presence of a second population.

We suggest four spectral regions that can be used in the studies of MPs in integrated light. Our proposed spectral indices seem to be a promising way of distinguishing populations in index-index diagrams, even in the presence of stochastic effects. For instance, we predict that our proposed OH_{blue}–NH_{blue} spectral index diagram is a strong indicator of the presence of a second population. We also investigated the behaviour of the chromosome maps when the colours are measured in the integrated light rather than in individual stars. We conclude that the second population may be detected with the following combination of colours: c(F275W, F336W, 438W) vs c(F275W, F438W, F814W).

By measuring spectrophotometric indices in pure 1P and 2P populations, we estimate the interval of possible values when a CNONa-anticorrelated population is present. In real-world GCs, a mixture of these populations or sub-populations will be present, and future work will be dedicated to disentangling these components in the integrated light.

Acknowledgements. This study was financed in part by the Coordenação de Aperfeiçoamento de Pessoal de Nível Superior – Brazil (CAPES) – Finance Code 88887.580690/2020-00 and by Agence Nationale de la Recherche, France, under project POPSYCLE (ANR-19-CE31-0022). We also acknowledge the support from Conselho Nacional de Desenvolvimento Científico e Tecnológico (CNPq) under the grants 200928/2022-8, 310555/2021-3, and 307115/2021-6, and from Fundação de Amparo à Pesquisa do Estado de São Paulo (FAPESP) process numbers 2021/08813-7 and 2022/03703-1.

References

Asplund, M., Grevesse, N., & Sauval, A. J. 2005, Cosmic Abundances as Records of Stellar Evolution and Nucleosynthesis, 336, 25
Asplund, M., Grevesse, N., Sauval, A. J., & Scott, P. 2009, ARA&A, 47, 481
Barbaro, C. & Bertelli, C. 1977, A&A, 54, 243
Bastian, N. & Lardo, C. 2018, ARA&A, 56, 83
Bertone, E., Chávez, M., & Mendoza, J. C. 2020, MNRAS, 493, 2195
Bragaglia, A., Carretta, E., Gratton, R., et al. 2010, A&A, 519, A60
Branco, V. 2020, Master's thesis, IAG – Universidade de São Paulo, Brazil, https://doi.org/10.11606/D.14.2020.tde-15122020-164651
Brault, J. W. 1985, in High Resolution in Astronomy, ed. A. O. Benz, M. Huber, & M. Mayor, 3–61
Brodie, J. P. & Strader, J. 2006, ARA&A, 44, 193
Bruzual A., G. 2002, in Extragalactic Star Clusters, ed. D. P. Geisler, E. K. Grebel, & D. Minniti, Vol. 207, 616
Carretta, E., Bragaglia, A., Gratton, R., & Lucatello, S. 2009, A&A, 505, 139
Carretta, E., Bragaglia, A., Gratton, R. G., et al. 2010, A&A, 516, A55
Carretta, E., Gratton, R. G., Lucatello, S., Bragaglia, A., & Bonifacio, P. 2005, A&A, 433, 597
Castelli, F. & Hubrig, S. 2004, A&A, 425, 263
Castelli, F. & Kurucz, R. L. 2003, in Modelling of Stellar Atmospheres, ed. N. Piskunov, W. W. Weiss, & D. F. Gray, Vol. 210, A20
Cerviño, M. 2013, New A Rev., 57, 123
Chung, C., Yoon, S.-J., Lee, S.-Y., & Lee, Y.-W. 2013, ApJS, 204, 3
Coelho, P., Barbuy, B., Meléndez, J., Schiavon, R. P., & Castilho, B. V. 2005, A&A, 443, 735
Coelho, P., Percival, S., & Salaris, M. 2012, in Astronomical Society of India Conference Series, Vol. 6, Astronomical Society of India Conference Series, ed. P. Prugniel & H. P. Singh, 107
Coelho, P., Percival, S. M., & Salaris, M. 2011, ApJ, 734, 72
Coelho, P. R. T. 2014, MNRAS, 440, 1027
Colucci, J. E., Bernstein, R. A., Cameron, S., McWilliam, A., & Cohen, J. G. 2009, ApJ, 704, 385
Colucci, J. E., Bernstein, R. A., & Cohen, J. G. 2014, ApJ, 797, 116
Colucci, J. E., Bernstein, R. A., & McWilliam, A. 2011, in American Astronomical Society Meeting Abstracts, Vol. 217, American Astronomical Society Meeting Abstracts #217, 328.04
Colucci, J. E., Bernstein, R. A., & McWilliam, A. 2017, ApJ, 834, 105
Cox, A. N. 2000, Allen's astrophysical quantities

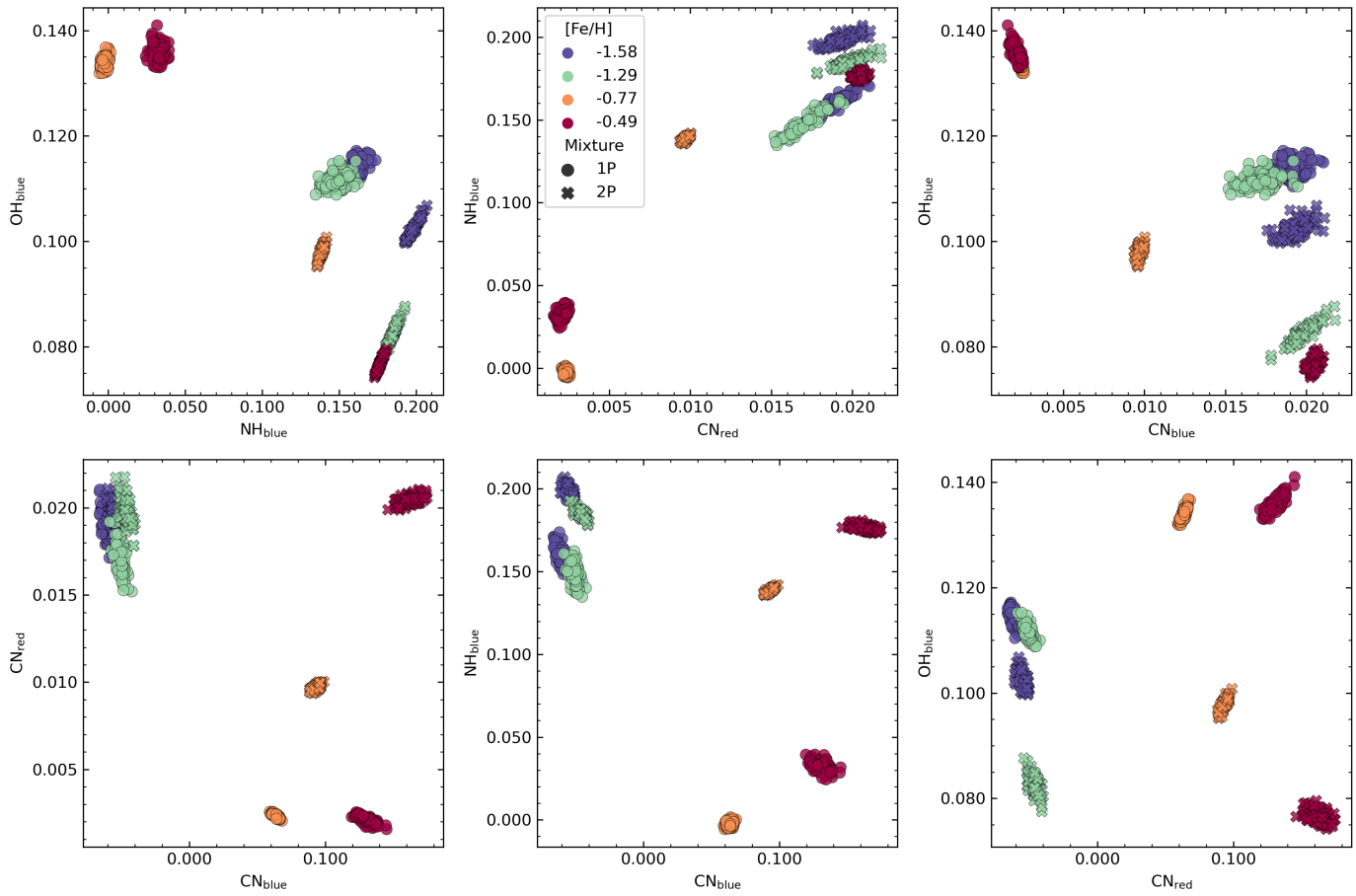

Fig. 7. Same as in Figure 6; this figure presents index-index diagrams showing the stochastic effects among the new indices proposed to be sensitive to the MP effects in GCs: OH_{blue}, NH_{blue}, CN_{blue}, CN_{red}.

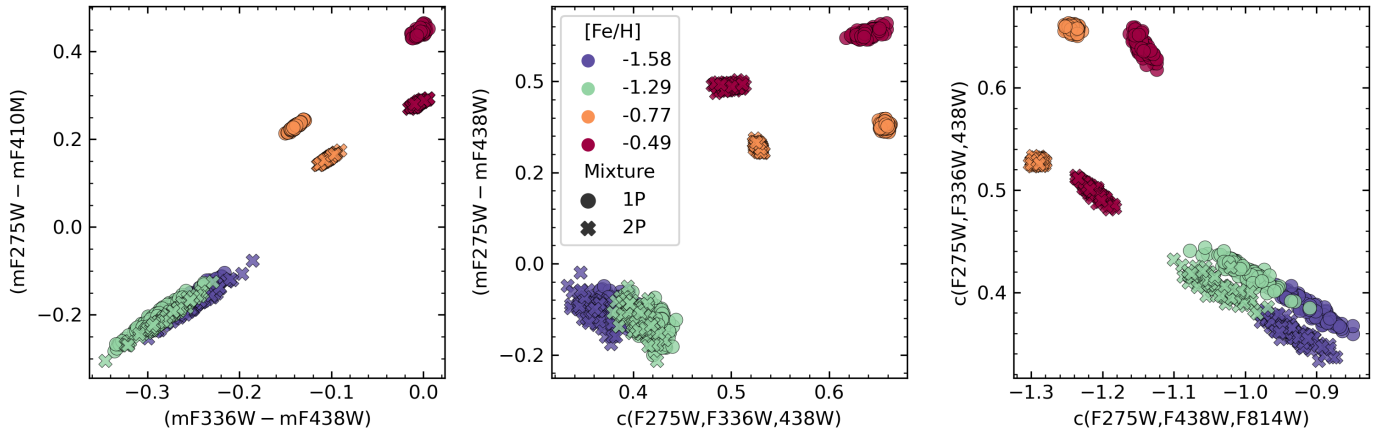

Fig. 8. Same as in Figure 5; from left to right, this figure presents a colour-colour and two Chromosome-maps diagrams.

da Silva, R. L., Fumagalli, M., & Krumholz, M. 2012, ApJ, 745, 145
D'Abrusco, R., Zegeye, D., Fabbiano, G., et al. 2022, ApJ, 927, 15
Dalessandro, E., Lapenna, E., Mucciarelli, A., et al. 2016, The Astrophysical Journal, 829, 77
D'Antona, F., Milone, A. P., Johnson, C. I., et al. 2022, ApJ, 925, 192
De Angeli, F., Piotto, G., Cassisi, S., et al. 2005, AJ, 130, 116
Dondoglio, E., Milone, A. P., Renzini, A., et al. 2022, ApJ, 927, 207
Dotter, A., Sarajedini, A., Anderson, J., et al. 2010, ApJ, 708, 698
Fouesneau, M. 2022, pyphot
Fouesneau, M. & Lançon, A. 2010, A&A, 521, A22
Franchini, M., Morossi, C., Di Marcantonio, P., et al. 2018, ApJ, 862, 146
Gilligan, C. K., Chaboyer, B., Cummings, J. D., et al. 2019, MNRAS, 486, 5581
Gontcharov, G. A., Bonatto, C. J., Ryutina, O. S., et al. 2023, MNRAS, 526, 5628
Gratton, R., Bragaglia, A., Carretta, E., et al. 2019, A&A Rev., 27, 8
Gratton, R. G., Carretta, E., & Bragaglia, A. 2012, A&A Rev., 20, 50
Grevesse, N. & Sauval, A. J. 1998, Space Sci. Rev., 85, 161
Harris, W. E. 1996, AJ, 112, 1487
Harris, W. E. 2010, arXiv e-prints, arXiv:1012.3224
Hidalgo, S. L., Pietrinferni, A., Cassisi, S., et al. 2018, ApJ, 856, 125
Hollyhead, K., Kacharov, N., Lardo, C., et al. 2017, Monthly Notices of the Royal Astronomical Society: Letters, 465, L39
Jang, S., Milone, A. P., Lagioia, E. P., et al. 2021, ApJ, 920, 129
Kraft, R. P. 1994, PASP, 106, 553
Kraft, R. P., Sneden, C., Smith, G. H., et al. 1997, AJ, 113, 279
Kroupa, P. 2001, MNRAS, 322, 231
Krumholz, M. R., McKee, C. F., & Bland-Hawthorn, J. 2019, ARA&A, 57, 227
Kurucz, R. L. 1970, SAO Special Report, 309
Kurucz, R. L. 2005, Memorie della Societa Astronomica Italiana Supplementi, 8, 14

Kurucz, R. L. 2018, Astronomical Society of the Pacific Conference Series, 515, 47
Kurucz, R. L. & Avrett, E. H. 1981, SAO Special Report, 391
Kurucz, R. L. & Furenlid, I. 1979, SAO Special Report, 387
Lagioia, E. P., Milone, A. P., Marino, A. F., & Dotter, A. 2019, ApJ, 871, 140
Lançon, A., Gonneau, A., Verro, K., et al. 2021, A&A, 649, A97
Larsen, S. S., Brodie, J. P., Grundahl, F., & Strader, J. 2014, ApJ, 797, 15
Larsen, S. S., Brodie, J. P., Wasserman, A., & Strader, J. 2018, A&A, 613, A56
Larsen, S. S., Eitner, P., Magg, E., et al. 2022, A&A, 660, A88
Lee, H. & Worthey, G. 2005, The Astrophysical Journal Supplement Series, 160, 176
Martins, L. P. & Coelho, P. 2007, Monthly Notices of the Royal Astronomical Society, 381, 1329
Martins, L. P., Coelho, P., Caproni, A., & Vitoriano, R. 2014, Monthly Notices of the Royal Astronomical Society, 442, 1294
Martins, L. P., Lima-Dias, C., Coelho, P. R. T., & Laganá, T. F. 2019, MNRAS, 484, 2388
Masseron, T., Plez, B., Van Eck, S., et al. 2014, A&A, 571, A47
McWilliam, A. & Bernstein, R. A. 2008, ApJ, 684, 326
Mészáros, S., Allende Prieto, C., Edvardsson, B., et al. 2012, AJ, 144, 120
Milone, A. P., Cordoni, G., Marino, A. F., et al. 2023a, A&A, 672, A161
Milone, A. P., Marino, A. F., Da Costa, G. S., et al. 2020, MNRAS, 491, 515
Milone, A. P., Marino, A. F., Dotter, A., et al. 2023b, MNRAS, 522, 2429
Milone, A. P., Marino, A. F., Piotto, G., et al. 2013, ApJ, 767, 120
Milone, A. P., Piotto, G., Renzini, A., et al. 2016, Monthly Notices of the Royal Astronomical Society, 464, 3636
Mucciarelli, A., Origlia, L., Ferraro, F. R., & Pancino, E. 2009, ApJ, 695, L134
Nardiello, D., Milone, A. P., Piotto, G., et al. 2018, MNRAS, 477, 2004
Niederhofer, F., Bastian, N., Kozhurina-Platais, V., et al. 2017a, MNRAS, 465, 4159
Niederhofer, F., Bastian, N., Kozhurina-Platais, V., et al. 2017b, MNRAS, 464, 94
Percival, S. M., Salaris, M., Cassisi, S., & Pietrinferni, A. 2009, ApJ, 690, 427
Peterson, R. C. & Kurucz, R. L. 2022, ApJS, 260, 28
Pietrinferni, A., Hidalgo, S., Cassisi, S., et al. 2021, ApJ, 908, 102
Piotto, G., Bedin, L. R., Anderson, J., et al. 2007, ApJ, 661, L53
Piotto, G., King, I. R., Djorgovski, S. G., et al. 2002, A&A, 391, 945
Popescu, B. & Hanson, M. M. 2010, ApJ, 724, 296
Sakari, C. M., Shetrone, M. D., McWilliam, A., & Wallerstein, G. 2021, MNRAS, 502, 5745
Sakari, C. M., Shetrone, M. D., Schiavon, R. P., et al. 2016, ApJ, 829, 116
Sakari, C. M., Venn, K., Shetrone, M., Dotter, A., & Mackey, D. 2014, MNRAS, 443, 2285
Sakari, C. M. & Wallerstein, G. 2022, MNRAS, 512, 4819
Salaris, M., Cassisi, S., Mucciarelli, A., & Nardiello, D. 2019, A&A, 629, A40
Salgado, C., Da Costa, G. S., Yong, D., et al. 2022, arXiv e-prints, arXiv:2202.00849
Saracino, S., Martocchia, S., Bastian, N., et al. 2020, MNRAS, 493, 6060
Sbordone, L. 2005, Memorie della Societa Astronomica Italiana Supplementi, 8, 61
Sbordone, L., Bonifacio, P., Castelli, F., & Kurucz, R. L. 2004, Memorie della Societa Astronomica Italiana Supplementi, 5, 93
Schiavon, R. P., Caldwell, N., Conroy, C., et al. 2013, ApJ, 776, L7
Schiavon, R. P., Caldwell, N., & Rose, J. A. 2004, AJ, 127, 1513
Thomas, D., Johansson, J., & Maraston, C. 2011, MNRAS, 412, 2199
Trager, S. C., Worthey, G., Faber, S. M., Burstein, D., & Gonzalez, J. J. 1998, ApJS, 116, 1
Usher, C., Pastorello, N., Bellstedt, S., et al. 2017, MNRAS, 468, 3828
VandenBerg, D. A., Edvardsson, B., Casagrande, L., & Ferguson, J. W. 2022, MNRAS, 509, 4189
Vazdekis, A., Sánchez-Blázquez, P., Falcón-Barroso, J., et al. 2010, MNRAS, 404, 1639
Walcher, C. J., Coelho, P., Gallazzi, A., & Charlot, S. 2009, MNRAS, 398, L44
Wallace, L., Hinkle, K. H., Livingston, W. C., & Davis, S. P. 2011, The Astrophysical Journal Supplement Series, 195, 6
Wheeler, J. C., Sneden, C., & Truran, James W., J. 1989, ARA&A, 27, 279
Worthey, G., Faber, S. M., Gonzalez, J. J., & Burstein, D. 1994, ApJS, 94, 687
Worthey, G. & Lee, H.-c. 2011, ApJS, 193, 1
Ziliotto, T., Milone, A., Marino, A. F., et al. 2023, ApJ, 953, 62

Appendix A: Molecular line lists

Molecular species used in all synthetic spectrum computation. TiO molecule is not present in the models with $T_{\rm eff} \geq 4500$ (K) due to computation time and weak effect in the final spectrum.

Table A.1. List of all molecular opacity species and files used in this work.

Molecule	Web address	File
AlH [A-X]	http://kurucz.harvard.edu/molecules/alh	alhax.asc
AlH [B-X]	http://kurucz.harvard.edu/molecules/alh	alhxx.asc
AlO	http://kurucz.harvard.edu/molecules/alo	alopatrascu.asc
C_2 [A-X]	http://kurucz.harvard.edu/linelists/linesmol	c2ax.asc
C_2 [B-A]	http://kurucz.harvard.edu/linelists/linesmol	c2ba.asc
C_2 [D-A]	http://kurucz.harvard.edu/molecules/c2	c2dabrookek.asc
C_2 [E-A]	http://kurucz.harvard.edu/linelists/linesmol	c2ea.asc
CaH	http://kurucz.harvard.edu/molecules/cah	cah.asc
CaO	http://kurucz.harvard.edu/molecules/cao	caoyurchenko.asc
CH	http://kurucz.harvard.edu/molecules/ch	chmasseron.asc
CN [A-X]	http://kurucz.harvard.edu/linelists/linesmol	cnax.asc
CN [B-X]	http://kurucz.harvard.edu/linelists/linesmol	cnbx.asc
CN [X-X]	http://kurucz.harvard.edu/molecules/cn	cnxx12brooke.asc
CO [A-X]	http://kurucz.harvard.edu/linelists/linesmol	coax.asc
CO [X-X]	http://kurucz.harvard.edu/linelists/linesmol	coxx.asc
CrH [A-X]	http://kurucz.harvard.edu/molecules/crh	crhaxbernath.asc
FeH [F-X]	http://kurucz.harvard.edu/molecules/feh	fehfx.asc
H_2	http://kurucz.harvard.edu/linelists/linesmol	h2.asc
MgH	http://kurucz.harvard.edu/molecules/mgh	mgh.asc
MgO	http://kurucz.harvard.edu/molecules/mgo	mgodaily.asc
NaH	http://kurucz.harvard.edu/molecules/nah	nahrivlin.asc
NH	http://kurucz.harvard.edu/linelists/linesmol	nh.asc
OH	http://kurucz.harvard.edu/molecules/oh	ohupdate.asc
SiH	http://kurucz.harvard.edu/linelists/linesmol	sihnew.asc
SiO [A-X]	http://kurucz.harvard.edu/linelists/linesmol	sioax.asc
SiO [E-X]	http://kurucz.harvard.edu/linelists/linesmol	sioex.asc
SiO [X-X]	http://kurucz.harvard.edu/linelists/linesmol	sioxx.asc
TiH	http://kurucz.harvard.edu/molecules/tih	tih.asc
TiO	http://kurucz.harvard.edu/molecules/tio	tioschwenke.asc
VO	http://kurucz.harvard.edu/molecules/vo	vo.asc

Appendix B: Spectral indices and photometry

All measurements in Table B.1 refer to the chemical mixtures and metallicities of the reference integrated spectra.

Table B.1. Spectral indices and colours of each reference integrated spectrum.

[Fe/H]	**-0.49**	**-0.49**	**-0.77**	**-0.77**	**-1.29**	**-1.29**	**-1.58**	**-1.58**
Mixture	1P	2P	1P	2P	1P	2P	1P	2P
CN_1	0.061	0.191	0.026	0.098	-0.037	-0.009	-0.049	-0.037
CN_2	0.107	0.239	0.065	0.139	0.005	0.030	-0.010	0.003
Ca4227	2.802	1.776	2.223	1.884	1.099	0.426	0.828	0.758
G4300	6.933	6.528	6.397	5.630	3.770	3.831	3.458	2.886
Na D	1.724	3.311	1.094	2.025	0.492	1.066	0.403	0.758
Fe5270	2.849	2.810	2.254	2.276	1.350	1.352	1.098	1.112
OH_{blue}	0.179	0.106	0.169	0.128	0.126	0.079	0.119	0.092
NH_{blue}	0.081	0.214	0.037	0.175	0.052	0.178	0.046	0.148
CN_{blue}	0.211	0.246	0.117	0.153	0.013	0.040	-0.008	0.005
CN_{blue}	0.000	0.025	0.000	0.012	0.004	0.013	0.004	0.007
[MgFe]	0.471	0.477	0.565	0.406	0.885	0.874	0.881	0.935
(mF336W – mF438W)	-0.251	-0.242	-0.289	-0.276	-0.124	-0.092	0.004	0.003
(mF438W – mF814W)	0.780	0.777	0.829	0.876	1.640	1.626	1.786	1.707
c(F275W,F336W,F438W)	0.376	0.347	0.412	0.397	0.651	0.522	0.636	0.494

Appendix C: Spectral indices proposed in the literature

Bertone et al. (2020) spectral indices were built upon stellar spectra. Therefore, we show in Figure C.1 how their proposed indices split the sub-populations when applied to the integrated light of a synthetic cluster. Table C.1 shows measurements of the reference integrated spectra.

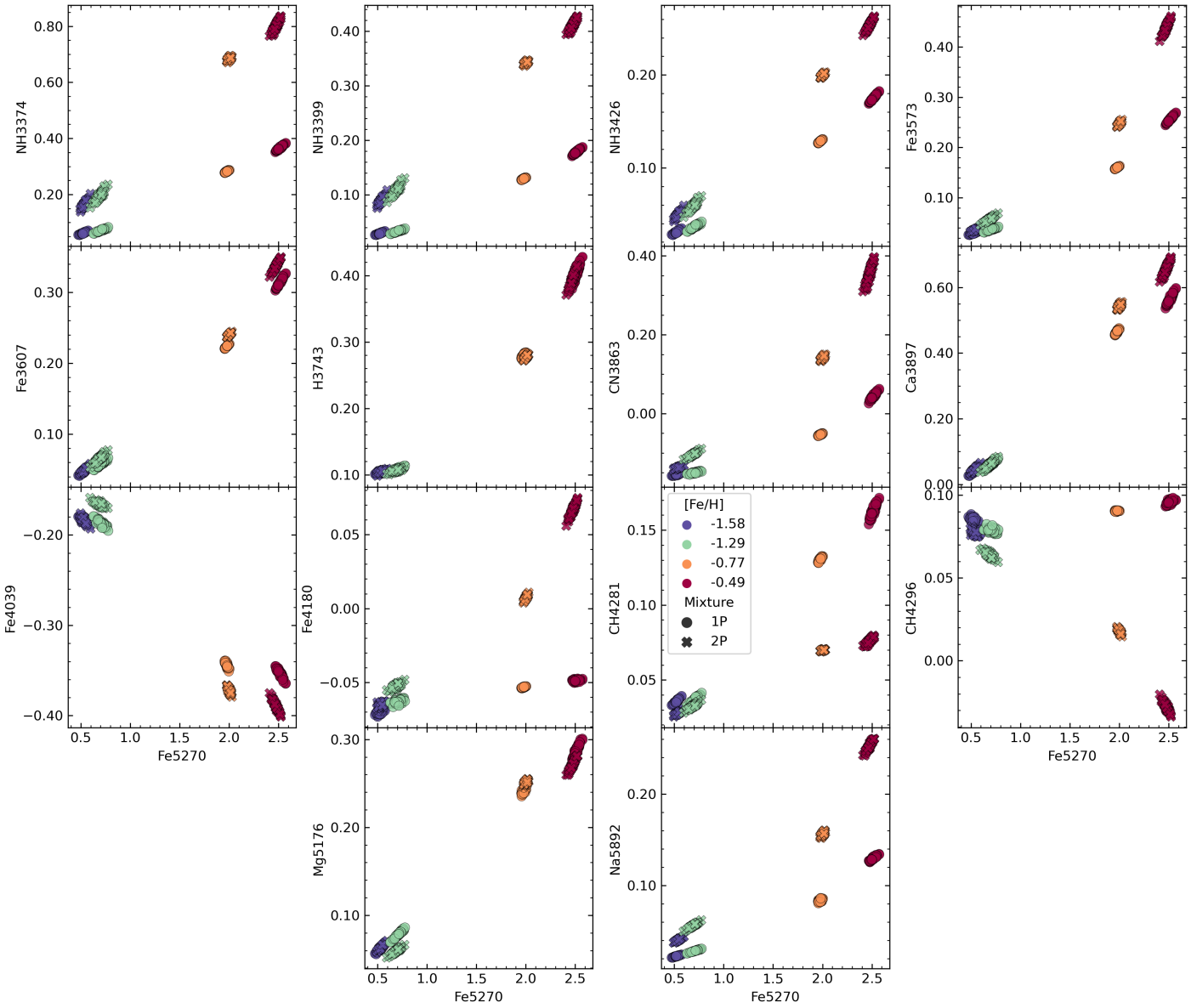

Fig. C.1. Diagrams with proposed spectral indices from the literature computed in the integrated light of different chemical mixture assumptions.

Table C.1. Bertone spectral indices measured with our reference integrated spectra.

[Fe/H]	**-0.49**	**-0.49**	**-0.77**	**-0.77**	**-1.29**	**-1.29**	**-1.58**	**-1.58**
Mixture	1P	2P	1P	2P	1P	2P	1P	2P
NH3374	0.445	0.898	0.350	0.765	0.192	0.511	0.172	0.449
NH3399	0.217	0.456	0.161	0.378	0.087	0.272	0.078	0.232
NH3426	0.218	0.304	0.159	0.234	0.087	0.146	0.075	0.125
Fe3573	0.329	0.581	0.203	0.335	0.090	0.167	0.071	0.096
Fe3607	0.381	0.415	0.269	0.289	0.136	0.156	0.110	0.116
H3743	0.513	0.506	0.341	0.330	0.170	0.168	0.140	0.139
CN3863	0.115	0.491	-0.010	0.239	-0.104	0.061	-0.106	-0.028
Ca3897	0.695	0.810	0.567	0.662	0.272	0.282	0.221	0.250
Fe4039	-0.413	-0.472	-0.396	-0.436	-0.273	-0.228	-0.244	-0.250
Fe4180	-0.031	0.126	-0.046	0.043	-0.047	-0.009	-0.048	-0.030
CH4281	0.181	0.077	0.153	0.075	0.089	0.072	0.086	0.058
CH4296	0.087	-0.069	0.093	-0.009	0.074	0.027	0.073	0.046
Mg5176	0.335	0.316	0.269	0.273	0.150	0.109	0.119	0.120
Na5892	0.157	0.305	0.104	0.187	0.049	0.098	0.040	0.071